Aerodynamics

Kristin Falk

Steven Wolhar

Jack Yovanovich

Mechanical

Matilda Chindasumpanda

Ethan Dinh

Kate Douglas

Ryan Hutchison

Jozhel Salazar-Espiridion

Bernie Tompkins

UT PROSIM

Power Systems and Controls

Scott Armand	Ishatva Jauhari
Sophie Atkisson	Carter Langley
Tim Brousseau	Tolu Kolade
Shiloh Carmack	Alessandro Martir
Noah Chin	Anna Ngo
Tamara Corvera-Andia	Charlotte Pei
Ethan Davidson	Vishnu Ramesh
Rachel Dean	Lucas Renfrew
Landon Ehrhart	Raman Rodman
Charlie Elliot	Karmick Surana
Advait Guje	Vedansh Tiwari
Melody Guo	Danny Warfield
Vivian Hazelrigg	Henry Warfield
Morris Jeong	Rakeb Yihunie

The Wind Turbine Team at Virginia Tech

Turbine Design Report

Collegiate Wind Competition 2026

Virginia Tech, Blacksburg, VA

Prototype Design Team

Dane Barnes | daneb@vt.edu	Mechanical Co-Lead
Louis Harris | hlouis@vt.edu	Aerodynamics Lead
Matthew Lewis | mlewis3113@vt.edu	Mechanical Co-Lead
Reve Meili | reve@vt.edu	Power Systems & Controls Co-Lead
Makeda Solomon | makedas@vt.edu	Power Systems & Controls Co-Lead

Faculty Advisors

Dr. Nanyaporn Intaratep | nintarat@vt.edu
Research Assistant Professor
Kevin T. Crofton Department of
Aerospace and Ocean Engineering

Dr. Tim Thacker | tthacker@vt.edu
Research Associate Professor
Bradley Department of Electrical &
Computer Engineering

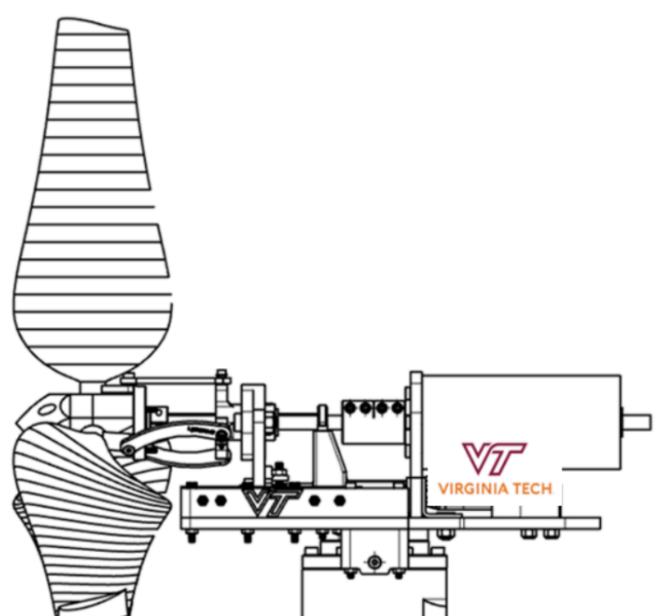

ENGINEERING VIRGINIA TECH.

Advanced Engineering Design Lab

COLLEGIATE WIND COMPETITION
U.S. DEPARTMENT OF ENERGY

1 Executive Summary

The Wind Turbine Team at Virginia Tech proudly designed a fully integrated small-scale wind turbine for the 2026 Collegiate Wind Competition. This system successfully converts wind energy into clean electrical power safely and efficiently, leveraging the skills of a devoted group of engineers in support of a brighter future.

To accomplish this outcome within the competition structure, blade design focused on maximizing power output over the range of competition wind speeds. The SG6043 airfoil was selected for its strong lift-to-drag ratio across a wide range of Reynolds numbers, and tip speed ratio (TSR) was configured for better cut-in. The pitch control mechanism was redesigned to improve pitch resolution, thereby supporting ideal rotor performance and control of RPM. A clamshell hub redesign and heat-set insert blade roots increased the allowable swept length of the blades, boosting performance. ASTM tensile tests were performed for PLA and PLA-CF at several infill levels to support engineering analysis of 3D-printed materials. All structures were designed to withstand significantly higher loads than those expected during the competition tasks.


Figure 1. Full System Assembly

The turbine's electrical system converts three-phase AC power from the generator into useful DC power using a diode-bridge rectifier. Schottky diodes are used to minimize voltage drop and improve efficiency at lower wind speeds. A capacitor, after rectification, smooths the DC output by reducing voltage ripple and stabilizing the bus. This provides a more consistent power supply for regulation and control systems. The Digitally Controllable Load (DCL) optimizes peak power by adjusting electrical resistance based on measured bus voltage to match the present wind conditions. Electrical isolation using optocouplers ensures safe and reliable operations while maintaining system control. The turbine control system uses a Finite State Machine (FSM) to manage operation based on the bus voltage and safety conditions across four stages: Cut-in, Power Curve, Rated Power, and Safety.

2 Technical Design

2.1 Design Objectives

After unexpected setbacks at the 2024-25 competition resulting in a last-place finish in the testing portion, the team decided to prioritize simplicity and functionality when making design decisions. Strategy surrounding scoring categories was identified early on in the project timeline and was addressed accordingly by the aerodynamic, mechanical, and electrical design. After analyzing last year's competition results, successful completion of all non-power-curve tasks was noted as a signifier of the divided upper tier of performers, whereas the power curve task was specifically used to rank teams in that tier. Due to this, the team focused heavily on building a system that can reliably score full points for the control of rated power, safety, and durability tasks, while maintaining a power curve performance of at least 20 points, in order to compete for a higher overall placement.

2.2 Adaptations from Previous Design

The current design builds on the efforts of previous years by retaining core elements that demonstrated stable and reliable performance while refining elements that limited control and efficiency. The blades use the same SG6043 airfoil as the previous year's competition, but the choice was not predetermined. Aerodynamic analysis of several candidate airfoils was performed and showed that the SG6043 remained the best choice for this year's design, and additional changes were made to improve performance. Without a foundation task, mechanical systems were fully redesigned to optimize rotor efficiency with less focus on nacelle weight reduction. The only legacy component included is the baseplate's turntable bearing, which was not replaced due to disproportionately high costs for a minimal change to the system. In the electrical design, the use of an AC motor, three-phase diode bridge rectifier, and smoothing capacitor system was retained to provide a stable PCC bus. These components were preserved due to their simplicity and consistent performance under variable operating conditions. The voltage-based code control method and relay-based load system were also maintained due to their robustness, predictable switching behavior and compatibility with the adapted load control strategy. Retaining these elements reduced design risk, allowing this year's design to focus on optimizing control and power regulation performance.

2.3 Aerodynamic Design

The primary goal of the aerodynamic design was to provide maximum efficiency across the range of competition wind speeds while enabling safe and reliable performance. Major design choices revolved around improving the overall blade efficiency at the most important competition wind speeds.

In order to determine the primary design parameters for the blades, the weighted average wind speed was calculated using the competition's wind speeds and weights for the Power Curve task to be around 7 m/s. In determining the optimal tip speed ratio, several airfoils were simulated across Reynolds numbers ranging from $1x10^3$ to $1.5x10^6$ using XFoil, to represent a range of performance characteristics. Low Reynolds number values are characteristic of the blade profile closer to the root, as well as at cut-in, when the combined velocity of the tunnel and of rotation seen by the airfoil is low. Higher Reynolds numbers are characteristic of the blade profile closer to the tip of the blade, where the same angular speed increases relative velocity seen by the airfoil significantly.

Analyzing this data (Figure 2) for the following airfoils: SG6043, A18, S1223, E64, and E387, shows that the SG6043 had the highest lift-to-drag ratio (L/D) performance across most of the range, especially at upper range of Reynolds numbers. This indicates a higher aerodynamic efficiency over the majority of the turbine's operating range. Additionally, the SG6043 maintains comparable lifting performance at the lower range of Reynolds numbers which represent cut-in, making it a desirable choice for its overall versatility.

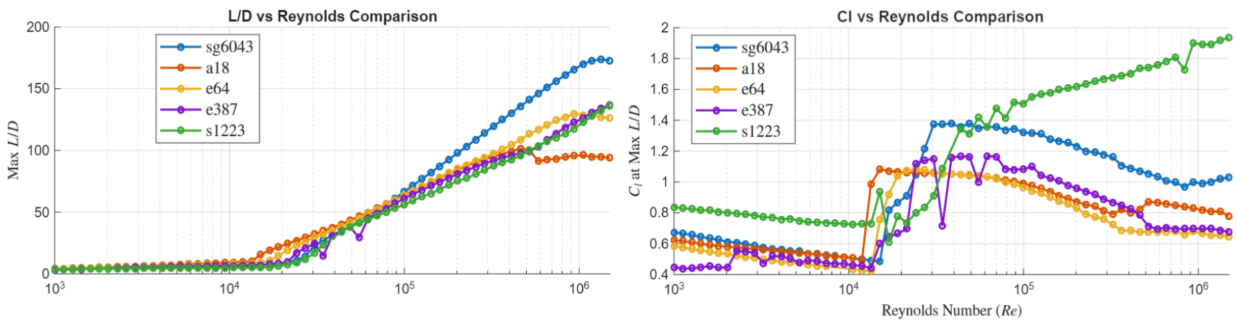

Figure 2. L/D vs Reynolds (left) and C_l vs Reynolds for Candidate Airfoils (right)

Because of its higher L/D performance over the majority of the turbine's operating range of Reynolds numbers, the SG6043 airfoil was then modeled at several design tip speed ratios using QBlade to determine the effect on the blade's overall maximum coefficient of power. Using this simulation, the SG6043 at a tip speed ratio of 4.1 was determined to be the best for power at the weighted average wind speed of 7 m/s. However, after wind tunnel testing of the prototype turbine, the blades did not reliably cut in before the first competition wind speed of 5 m/s. Because of this low cut-in performance, the design tip speed ratio was lowered from 4.1 to 3.7 to reduce cut-in speed from ~5.6 m/s to ~4 m/s. This meant that the rotor would reliably be spinning once the tunnel reached the first operating wind speed of 5 m/s, improving overall consistency at the cost of some theoretical performance in the higher end of the range.

Comparing the performance of this year's turbine to blades tested during the 2024-2025 competition using the same generator and load system, this year's turbine generated noticeably more power across the range of wind speeds. Figure 3, shows, using third-order curve fits of the raw data, comparison between this year's power curve with the final blade design with the winglet, and blades from the previous year's competition. Both testing setups used an identical Maxon 634043 generator, rectifier, capacitor, and 5 ohm electrical load, meaning difference in results can be directly attributed to changes in rotor design. Improvement in the current power curve was significant in the lower range before 7m/s, resulting in an overall 64% increase in the expected amount of power curve points, when assigning the competition weightings for this year to the powers generated at the competition wind speeds. The improvement comes in part from mechanical design changes that allowed the blade profile to extend closer to the root, enabling an increase in total swept area of the blades. Additionally, greater precision of the pitch control system allows airfoils to reach closer to their theoretical max L/D performance much more reliably, resulting in efficiency gains across the wind speed range.

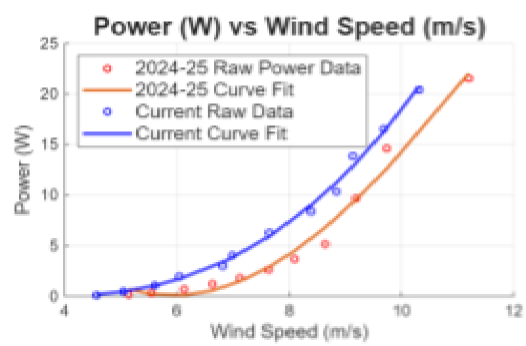

Figure 3: 2024-25 Rotor Performance vs. Current Rotor Performance (5 ohm Load)

In designing small-scale turbine blades, a major source of aerodynamic losses occurs at the blade's tip through the generation of tip vortices that significantly increase drag. After investigating strategies to reduce these tip vortex losses, the addition of a winglet on the end of the blade became a promising option. Following winglet geometry research (Mourad, et al. 2019, Khaled et al. 2019), winglet geometry parameters were designed to be 6% of rotor length, with a 48.3 degree cant angle, and a 20 degree toe angle. The twist and chord distribution of both blades was calculated using QBlade's built in optimization, using a design tip speed ratio of 3.7, an optimal L/D at 8.5°. Both twist and chord distributions were optimized with the Schwartz method available in QBlade because it creates much more physically realistic cross sections near the root than the Betz method in QBlade.

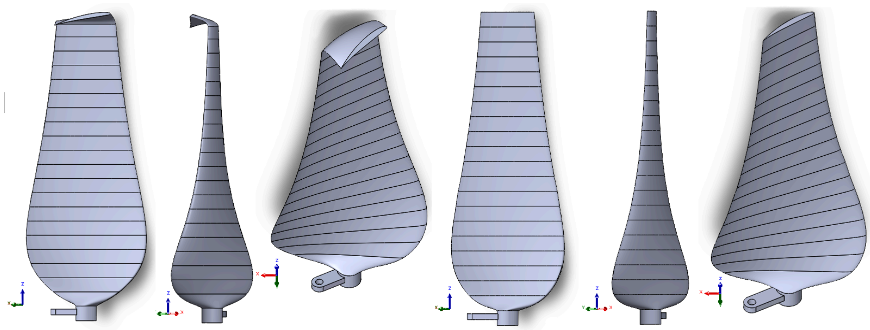

Figure 4: Blended Winglet Blade vs. No Winglet Blade

Testing both the winglet blade and the no-winglet blade across the range of wind speeds for power led to inconclusive results. The power generated across wind speeds was similar in wind tunnel testing, despite theoretical improvements for the winglet. In order to fully characterize winglet performance in the future, more precise testing data across a wider range of wind speeds, along with computational fluid dynamics simulations comparing different designs is required.

2.4 Mechanical Design

2.4.1 System Overview

The mechanical system addresses the team's overarching objectives by providing a structurally sound platform for the blades and electronics to efficiently perform all competition tasks. Major design choices were focused on optimizing pitch precision and rotor performance.

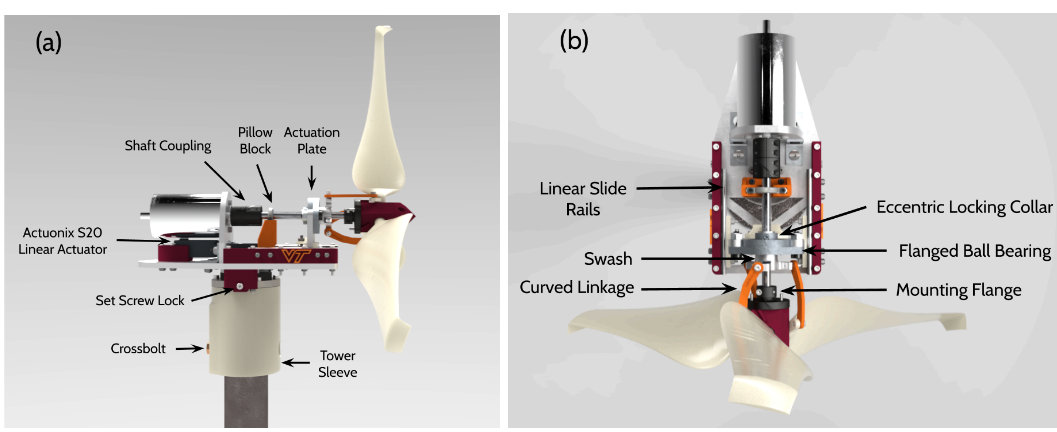

Figure 5. (a) Side View of Nacelle Assembly, (b) Top View of Nacelle Assembly

Nacelle structures are located atop the carbon steel tower and secured by a crossbolt that compresses the face of the PLA tower sleeve and the opposite face of the tower. This sleeve is fitted with heat-set inserts to mount the outer housing of the turntable bearing beneath the baseplate. While this bearing allows the baseplate to rotate freely during installation, two PLA set screw locks with heat-set inserts are outfitted with screws to prevent yaw during operation. An Actuonix S20 linear actuator is raised above the surface of the aluminum baseplate and passes through a PLA pillow block before interfacing with an aluminum actuation plate, which is laterally supported by steel linear slide rails. The pillow block locates a housed ball bearing supporting the driveshaft. A flanged ball bearing is joined to the actuation plate, and an aluminum swash is fixed to the inner race of the flanged bearing by an eccentric collar and set screw. As the swash actuates, a set of curved linkages pitch the blades simultaneously.

The primary goal of the pitch control system was to precisely orient the blades such that L/D is maximized during the power curve task, and RPM is safely monitored during the control of rated power, safety, and durability tasks. System changes resulted in a pitch resolution of 0.035 degrees per pulse of the actuator, 99% smaller than the previous system's value of 3.9 degrees per pulse. Calculations assumed linear translation of the swash is directly proportional to rotation of the blades. The extremely small step size of the stepper linear actuator (0.01 mm) was verified in testing and made a much finer resolution possible.

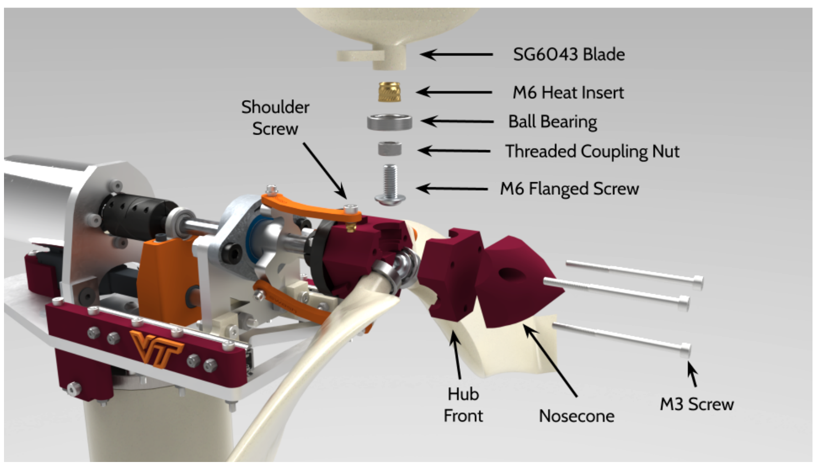

Figure 6. Hub Assembly

The hub assembly was designed to accommodate blades with a longer swept length by minimizing the radial dimension of non-blade components. Hub structures were printed in PA6-CF20 nylon to maintain strength and rigidity while allowing for complex geometries. The hub is partially seated on the keyed driveshaft and fastened to the steel mounting flange by screws which clamshell the hub housings and nosecone. Roots of each PLA-CF blade are fitted with heat-set inserts and fastened to the top face of a ball bearing by a flanged screw, which is retained by the inner race of the bearing. Blade linkage arms are also fitted with heat-set inserts and shoulder screws to interface with the pitch linkages. A coupling nut matching the inner diameter and width of the ball bearing is tightened to the screw for stability. Blade roots are housed and retained by the hub through contact on the outer race of the bearings.

Table 1. Hub and Blades System Comparison to Previous Design

Competition Year	Allowable Swept Length of Blade (mm)	Total Mass of Assembly (g)	Mass Moment of Inertia about Driveshaft (kg mm^2)

2024-25	190.2	329	380
2025-26	202.1	272	419

Masses were measured manually first, then applied in CAD to find inertia using Onshape's mass and section properties tab. Hub size reduction efforts resulted in a ~6.3% increase in the allowable swept length of the blades (Table 1). Changing hub material from machined aluminum to PA6-CF20 filament greatly reduced the total mass of the assembly, and made the increased mass moment of inertia caused by greater blade mass less significant. The team determined through testing that this inertial tradeoff was clearly outweighed by the performance of the new blades.

2.4.2 Mechanical Loads Analysis

To enable more accurate engineering analysis of 3D-printed materials and inform best practice printing parameters, the team conducted extensive ASTM tensile testing.

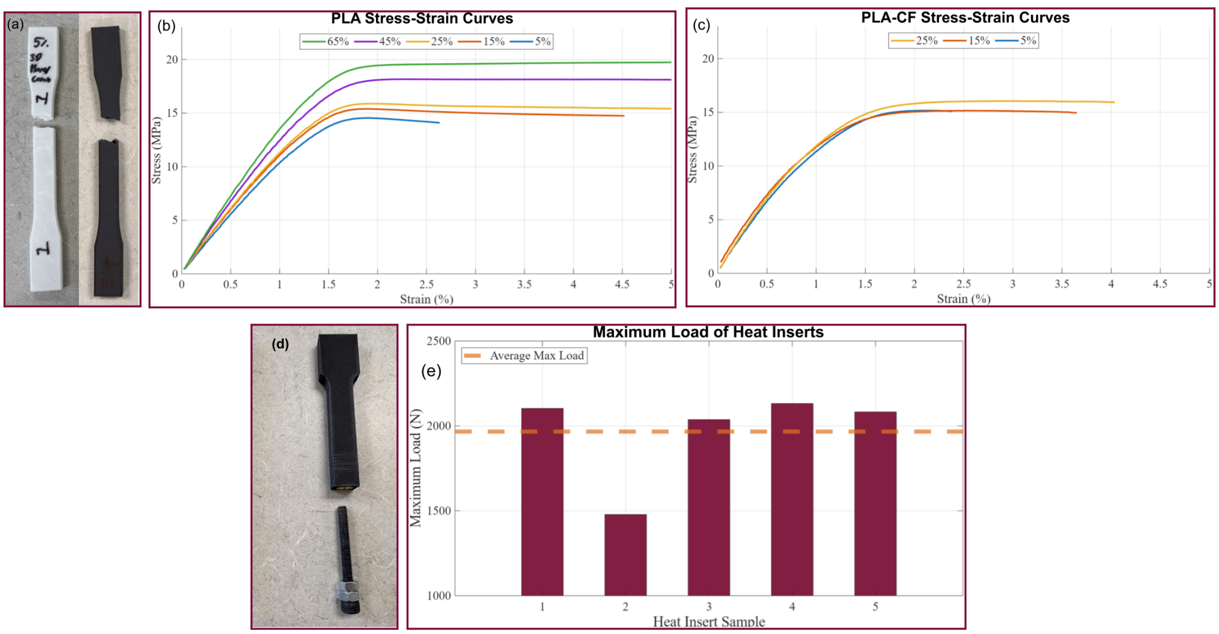

Figure 7. (a) PLA-CF ASTM Type-I sample (left) and PLA-CF ASTM Type-I sample (right), (b) PLA Stress-Strain data, (c) PLA-CF Stress-Strain data, (d) Heat Insert sample, (e) Heat Insert maximum force data

Five samples were tested for each infill value. M6 Heat inserts were tested by fastening a screw to the insert and securing it in the clamp opposite the sample. Data gathered from PLA dogbone samples led the team to print PLA structures using 25% infill due to its balance of weight/material efficiency while still offering a suitably high average yield strength of 15.56 MPa. PLA-CF demonstrated its value for low-infill, high-stiffness structures like the blades, which are intended to be as lightweight as possible within structural safety constraints. Heat insert samples averaged a pull-out force of 1967 N, and showed the strength defects of suboptimal insert installation in Trial 2.

The blade roots were quickly identified as a critical component of the system given the significant operational centrifugal loads acting on tight stress concentrations in the root geometry. To model load interactions, finite element analysis was conducted in ANSYS (Figure 8).

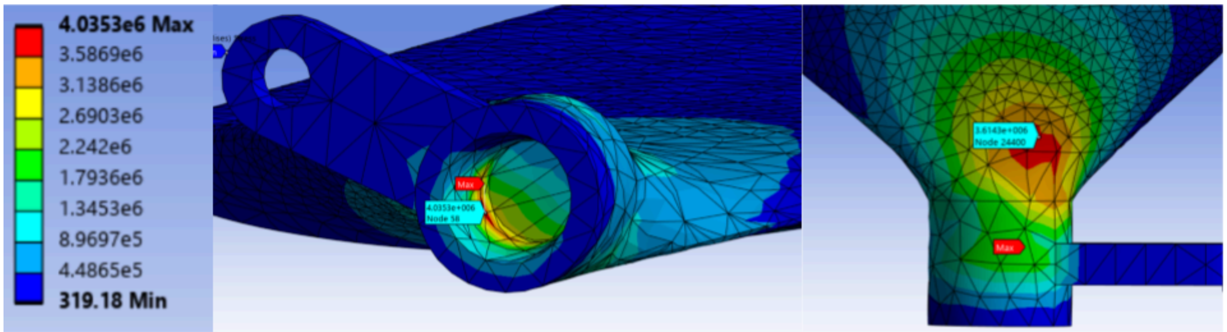

Figure 8. Von-Mises Equivalent Stress on Blade

A custom material assignment was given to the blade using PLA-CF material properties found from tensile testing. An angular velocity condition about a local coordinate axis 14 mm below the blade was applied to simulate rotation about the driveshaft axis, while a fixed support was applied to the inner face of the root to resemble the heat-set insert. Equivalent stresses of 4.04 MPa and 3.61 MPa were found at critical locations inside the root and at the transition point of the blade respectively. The safety factor tool was used to find associated safety factors of 3.86 and 3.94 for these two areas. The force reaction tool found maximum force in global coordinate directions: 1.0 N (x-axis), 0.85 N (y-axis), and 120 N (z-axis). This z-axis force component was comparable to the team's calculated centrifugal force of 108 N, which was based on real-world center-of-mass measurements with a 4 mm wide fulcrum. This information, combined with heat-set insert testing, suggests that the blade is likely to fail before tear-out of the insert (heat-set inserts display a tear-out factor of safety of 16.4). Inertial results were additionally used for the equivalent radial load acting on the blade bearings and combined loading on the hub.

A defeatured rendition of the driveshaft under operating conditions was modeled with KISSsoft's shaft and bearings package to assess equivalent radial loads along the drivetrain (Figure 9). Included in this model was the maximum experimental torque based on tested maximum power output and angular velocity data at 10 m/s wind speed assuming an electrical efficiency of 90%, which resolved to a 0.1595 Nm driving and driven torque on respective ends of the shaft (assuming a constant angular velocity of 1600 RPM). The shaft coupler was treated as part of the driveshaft and driven torque was assigned to the motor. The hub and blades were represented by the driving torque and a -2.67 N centrical load applied to the cantilevered edge of the shaft, and ball bearings were placed in the pitch configuration of peak power at 10 m/s. Custom material, surface finish, and keyway features were assigned to the shaft.

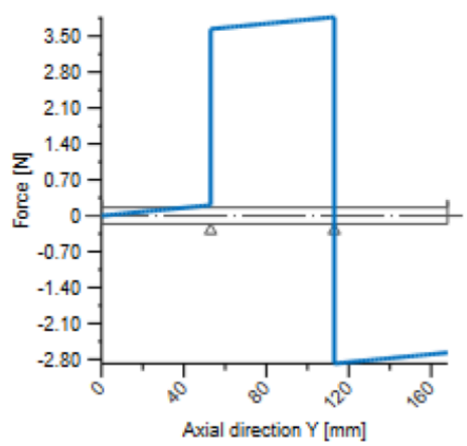

Figure 9. Shear Force vs. Axial Location in KISSsoft Shaft Modeling Software

This process defined -3.42 N and 6.75 N reaction forces acting at the pillow block bearing and actuation plate bearing respectively. These loads were used to find safety factors for related support structures in ANSYS. Results also justified the use of the actuation plate, which was designed to remove side loading on the linear actuator as much as physically possible. According to the datasheet, the maximum push force of the actuator at a desired actuation speed of 10 mm/s is approximately 15 N, which correlates to a maximum side load of 1.5 N (Actuonix Motion Devices Inc. 2020) - far below the radial force applied by the driveshaft.

Actuator push force is doubly relevant when considering thrust loads acting on the system. To verify the actuator can function properly during rated operation, power coefficient (C_P) of the rotor at 10 m/s wind speed was calculated using the maximum measured power output of the generator, assuming 90% electrical efficiency and a 45 cm diameter circular rotor cross-section. From there, axial induction factor (α) was derived and re-applied to find thrust coefficient (C_T) and ultimately thrust force. A thrust force of 6.49 N on the rotor was calculated, which is reacted to independently by the linear actuator, which maintains the angular position of the blades, and the shaft coupling, which constrains axial motion of the driveshaft. Combined axial and radial loading on the actuation bearing while pitching was integrated when assigning an operational safety factor for the bearing.

Using MATLAB programming, tower thickness and material were chosen based on a conservative natural frequency equation that models the tower as a cantilevered hollow cylinder with an oscillating tip mass. The calculated natural frequency of the new tower was roughly 3750 RPM, which falls safely above the expected operating range.

Table 2. Summary of Safety Factors

Component	Failure Mode	Safety Factor (10 m/s Wind Speed)	
		Operating Conditions	Parked Conditions
Blade Bearing	Fracture	3.34	400
SG6043 Blade	Fracture	3.86	21.3
Actuation Plate Mount	Fracture	10.3	15.4
Linear Actuator Adaptor	Fracture	10.6	39.1
M6 Heat-set Insert (Blade)	Tear-out	16.4	4180
Slide Rails	Wear	26.4	39.6
Hub Housing	Fracture	36.9	3560
Linkage	Fracture	76.2	97.9
Tower Sleeve	Fracture	251	264
Actuation Bearing	Fatigue, Fracture	420	511

Safety factors for all primary components are shown in Table 2. Fasteners and metal structures are generally excluded for clarity as they display extremely high safety factors. Bearing calculations used SKF's general bearing load guidelines when bearing catalogue information was unavailable. Operating status assumes the turbine maintains constant angular velocity at rated power (1600 RPM). Parked status assumes the turbine has entered safety mode and blades are pitched perpendicular to wind direction (0 RPM).

2.5 Electrical Design

The electrical system consists of the generator, turbine-side box, and load-side box. The turbine-side and load-side electronics are electrically isolated for safe and reliable operation. The turbine side electronics include the rectification stage, linear actuator driver, DC-DC converter, and safety system, while the load side consists of a digitally controllable load (DCL), control hardware, and communication interfaces.

2.5.1 Generator Selection

Two generators were selected for evaluation based on the demonstrated performance of the EC-i Maxon generators in prior implementations– the Maxon 633919 and the Maxon 634043. Key selection criteria included voltage output characteristics, efficiency at low rotational speeds, and compatibility with the DC-DC converter and controls. A steady-state equivalent generator model was implemented in MATLAB to compare the performance of the two generators over the expected operating range of 450 to 1300 RPM. Three key performance metrics were evaluated: open-circuit voltage, ideal matched-load power, and maximum continuous output power. The results indicate that the Maxon 634043 produces a higher open-circuit voltage across the full speed range due to its larger back-electromagnetic force constant (Maxon Group, 2026). Under ideal matched-load conditions, the same generator achieves a higher theoretical maximum power. The maximum continuous output power was evaluated while enforcing each generator's continuous current limit, for the purposes of a more practical comparison, illustrated in Figure 10. Under these conditions, the 634043 performs better at lower wind speeds because it generates higher voltage per RPM. In comparison, the 633919 becomes more competitive at higher speeds because it can deliver a larger continuous current.

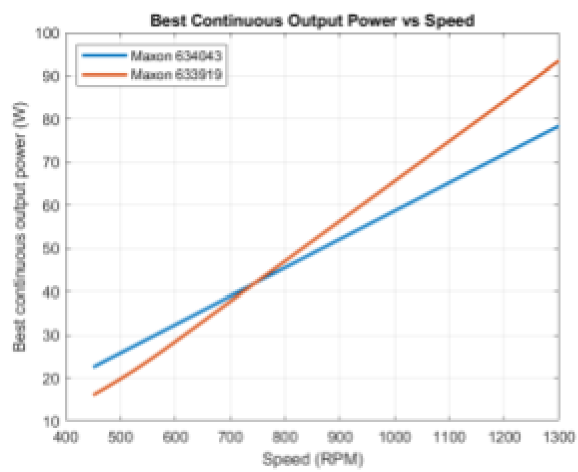

Figure 10. Continuous Output Power Comparison of Generators

This trend indicates that neither generator is universally superior under all conditions; however, when testing the generators, the Maxon 633919 demonstrated greater compatibility with the control of rated power requirement. To fulfill the requirement, a DC-DC converter is connected to the load, which draws significant current from the point of common connection (PCC). Due to the 633919's higher maximum continuous current, the generator was able to sustain a much higher stable output power than the 634043. Results demonstrate that the 633919 could sustain a greater current draw at higher speeds while minimizing the amount of load switching required, thereby simplifying controls and justifying the implementation of the Maxon 633919.

2.5.2 Turbine Side Electronics

The electrical system converts mechanical energy from the turbine into regulated DC electrical power across a range of wind conditions while regulating voltage below the 48 V limit at PCC.

One of the design methods for power analysis was to compute a load analysis of each component within the turbine-side enclosure. Previous system iterations indicated that the cumulative electronic load could significantly influence the PCC bus, occasionally impacting the behavior of the backfeed system and contributing to unintended operating conditions. To address this, the team performed a comprehensive load analysis of all electronics connected to the turbine bus with the intention to reduce the loading. Table 3 summarizes the components within the turbine-side enclosure along with their maximum current demands on the PCC bus. Entries marked with dashes indicate negligible impact on the system.

Table 3. Load Analysis of Turbine Side Electronics

Component	Function	Operating Voltage (V)	Current Draw (A)	Efficiency
Tic T825	Linear actuator driver	8.5-45V	0.55-0.6A	Variable
Pololu Voltage Regulator	DC/DC regulation	2.9-32V input / 9V output	0.1-0.5A	80% - 90%
LM5118EVAL	DC/DC converter	5-75V input / 12V output	up to 3.5 A	85%
3-Phase Bridge Rectifier	AC to DC conversion	3ϕ AC	—	< 92%
Shorting Relays	Fail-safe system	12V	0.007-0.009A	–
STPS5L60 Schottky Diode	Backfeed system	–	–	< 92%

The team avoided a microcontroller or additional buck-boost converters on the turbine side to step down the voltage for various equipment. Hence, the team opted for the Pololu Voltage Regulator with a 9V output as it could handle a wide voltage input range to power the linear actuator driver and the relays to prevent any possible damage to the low-voltage equipment, as well as provide a constant and stable voltage reading for the electronics. A critical component when analyzing the loading of PCC was the Tic T825 driver. The Tic T825 is responsible for driving the Actuonix S20 linear actuator, which has a phase resistance of 6.5 Ω/phase with a rated phase current of 0.6 A per phase. Hence, the Tic T825 was configured to 0.608 A per phase to provide just enough current to drive the actuator. By using the 0.608 A/phase setting:

$$P_{phase} = I^2R = (0.608)^2(6.5) = 2.4\,W\ for\ one\ phase\ energized \quad (1)$$

Hence, the driver, configured to 608 mA per phase, draws approximately 0.55 A from the 9 V regulated supply under two-phase operation, corresponding to approximately 4.8 W of loss if operating continuously. However, this is a maximum approximation, as the phases will not be energized for the entire duration of testing. Another critical component when analyzing the loading of PCC was the LM5118EVAL DC-DC converter, which outputs a constant 12V, and loads down the bus heavily when activated by drawing up to 3.5 A. The decrease in current draw on the turbine side compared to last year will help decrease the loading of the PCC bus and backfeed complications when the system is active.

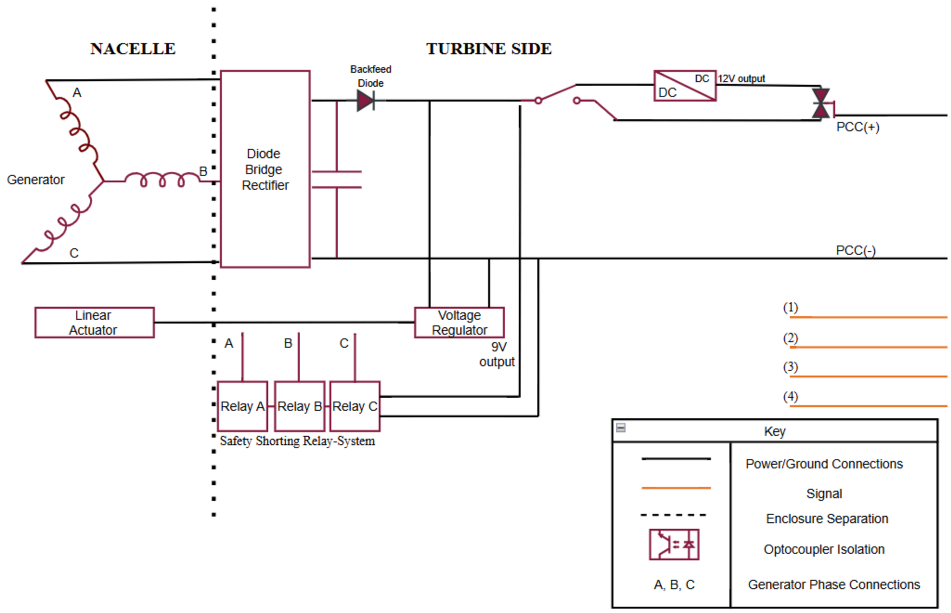

Figure 11. Turbine Side One-Line Diagram

Figure 11 illustrates the electrical system architecture of the turbine side enclosure. A diode bridge rectifier was implemented to convert the three-phase AC power to DC. The rectification stage was implemented on a custom printed circuit board (PCB) to optimize organization, durability, and integration. Schottky diodes replaced standard diodes to reduce forward voltage drop to 0.2-0.4V and improve efficiency, especially at lower operating voltages. Following the rectification bridge, two capacitors within the 10 J limit ensure smoothing of the voltage ripple and act as additional support for turbine side electronics in the case of a low voltage condition.

The Pololu voltage regulator acts as a buck-boost converter to a constant 9V output to power the Tic T825 linear actuator driver and additional relays (Pololu, 2026). The Pololu voltage regulator was chosen due to its wide operating voltage range, which allows the turbine-side electronics to function at low wind speeds.

The linear actuator is driven by a Pololu Tic T825 USB Multi-Interface Stepper Motor Controller. These components were selected for the precise control of current and flexible interface options, such as I2C and STEP/DIR communications. The driver enables direct integration with the microcontroller while providing built-in safety features that improve system reliability.

A DC-DC converter was implemented this year to satisfy the control of rated power requirement by regulating output voltage, so the turbine can operate safely around its rated power under varying wind conditions. The converter is selectively enabled using a relay, allowing it to be engaged only when the turbine enters rated power operation after 10 m/s. At this stage, the generator can supply enough current for the DC-DC converter to operate at. The switching relay allows for the system to operate efficiently in low-wind conditions without converter losses while providing regulation at higher wind speeds.

Safety is an essential element to ensure the turbine can survive a critical failure that would otherwise threaten the long-term functionality of the system. To address the load disconnect requirement, a three-relay circuit is used to short through impedances to limit the maximum current to the generator phases, increasing electromagnetic torque and rapidly decelerating the rotor.

2.5.3 Load Side Electronics

The load-side enclosure serves as the primary interface between the turbine and the external electrical load, enabling controlled power delivery, system monitoring, and protective actions during operation in response to operating conditions. Figure 12 shows the load side electronics. The load-side system is responsible for managing how power from the PCC bus is routed to the load, while also supporting the control hardware used to regulate turbine behavior.

A single Arduino R4 microcontroller was selected to handle control logic, relay switching, and monitoring of the PCC bus voltage. Compared to prior implementations using the dual-microcontroller architecture, consolidating these functions into a single controller improves synchronization, reduces communication overhead, and enhances overall system stability.

To maximize power across varying wind speeds, a DCL was implemented using a relay-based network. The microcontroller monitors the PCC voltage–which represents specific wind speeds and actuates relays based on predefined voltage thresholds. This element was initialized with four relays to switch between combinations of four corresponding resistor branches in parallel. By enabling different combinations of resistors, the system achieves a range of equivalent resistances to adjust the power being drawn based upon wind speed and system conditions. Lower resistance increases current draw and electromagnetic torque, slowing the turbine, while higher resistance allows increased rotational speed. Optimal resistance values for each wind speed were found experimentally, concluding that the most optimal selection was 50 Ω, 20 Ω, 10 Ω, and 5 Ω, providing sufficient resolution across the desired operating range. Relays were selected over MOSFET-based switching due to their robustness. Relays are less susceptible to voltage spikes and thermal runaway, making them more reliable under the transient conditions produced by a generator compared to MOSFETs.

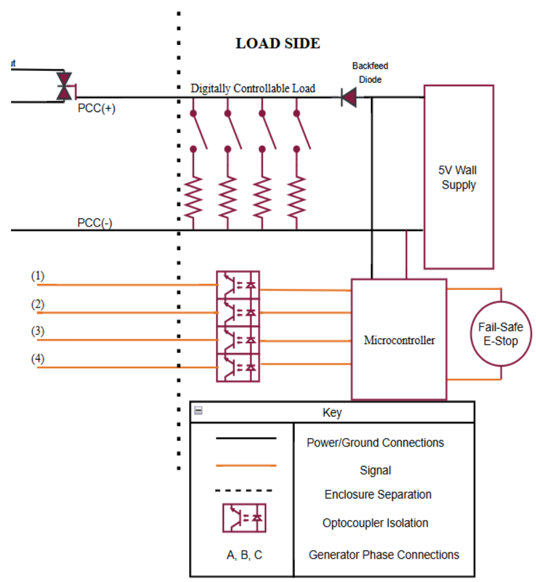

Figure 12. Load Side One-Line Diagram

To simplify the electrically isolated communication requirement, optocouplers were implemented in place of wireless communication modules, providing a simple and reliable hardware solution without additional software overhead. Pull-up resistor configurations are used on the output side of the optocouplers to ensure proper signal interpretation by the microcontroller. Optocouplers achieve electrical isolation by using internal LEDs to transfer signals between two isolated circuits. Figure 12 highlights the four signal wires sent to the turbine box with the following purposes: (1) represents step control of the driver, (2) direction control of the linear actuator, (3) control of the relay selecting between PCC paths, and (4) control of the safety system under complete isolation.

2.5.4 Controls and Software Validation

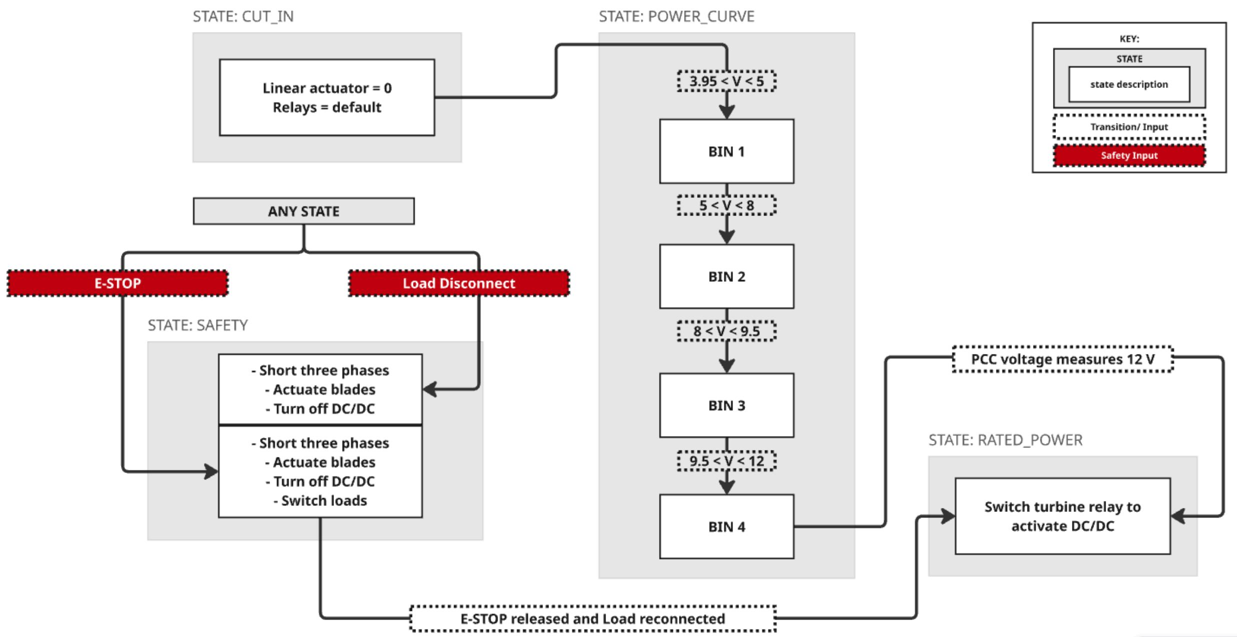

Figure 13. Diagram of the FSM Architecture

The control system regulates turbine operation by coordinating blade pitch, discrete resistive load selection, and DC-DC power regulation using measured bus voltage and safety inputs. A finite state machine (FSM) manages four operating states: CUT_IN, POWER_CURVE, RATED_POWER, and SAFETY, illustrated in Figure 13. Bus voltage is the primary feedback signal for operating-state decisions, while protection logic continuously monitors safety conditions and can preempt any active state. Initially, the turbine enters CUT_IN to initialize all parameters (setting default relay settings and linear actuator to zero). The turbine then immediately transitions to POWER_CURVE, where voltage-bin logic updates both actuator target position and load setting across the cut-in to rated-power region. As the bins increase, the load changes and the linear actuator steps forward. When bus voltage exceeds the rated-entry threshold for the required dwell time (value determined to be 12 V during testing to represent the 10 m/s wind speed), the FSM enters RATED_POWER, enables the DC-DC relay, applies the rated load setting, and holds the pitch to a constant position, all with the purpose of satisfying the constant power expectations at 10 m/s and on. If a protection trip occurs, the FSM enters SAFETY, disables the DC-DC relay, applies the safety dump load, and commands the linear actuator to the predefined safety position. After the trip condition is cleared for the restart dwell period, operation resumes by re-entering RATED_POWER.

The control system was validated through wind tunnel testing by monitoring state transitions, voltage thresholds, and system response under varying wind speeds. The FSM behavior was verified by confirming correct transitions between CUT_IN, POWER_CURVE, RATED_POWER, and SAFETY states based on measured bus voltage and fault conditions.

3 Final Assembly and Commissioning

3.1 Turbine Subsystems

The turbine consists of five overarching subsystems: the blades, hub, pitch control, generator, and tower. These subsystems are split into three main subteams: Aerodynamics (blades), Mechanical (hub, pitch control, and tower) and Power Systems and Controls (generator). This structure allows students of various engineering disciplines to directly apply concepts from their curriculum in a practical context. The team held weekly general body meetings and isolated subteam meetings to ensure fluent collaboration and mutual progress across the subsystems.

3.2 Assembly & Commissioning Checklist

Before beginning the 5-minute installation phase, the team will undergo a pre-assembly process as follows: The team will mate the tower sleeve and turntable bearing, and fasten baseplate structures including the pillow block assembly, slide rail assembly, set screw locks, and generator mounting plate. The generator will be held and its phase connectors threaded through the middle of the baseplate and spacer and into the tower sleeve through the bearing. The baseplate and spacer are fastened to the bearing, and the linear actuator connectors are also threaded through before the linear actuator is mounted. Once all wires are accessible through the tower sleeve, the shaft coupling is placed in its desired position while the generator is fastened. Then, the driveshaft, with swash, actuation bearing, and linkages attached, is led through the pillow block bearing and clamped by the shaft coupling. The actuation bearing is fastened to the actuation plate. The clamping flange is added to the driveshaft before the rest of the hub/blade assembly, and the two are fastened. Once this process is complete, the team is ready to begin installation.

Table 4. Commissioning Checklist

Commissioning Step	Check 1	Check 2
Pass turbine side connectors through the underside of the tunnel flange		
Orient tower above base mounting studs		
Pass turbine side connectors through the body of the tower		
Place the tower onto base mounting studs and fasten wingnuts		
Mate generator and linear actuator cables from the turbine-side enclosure to the nacelle		
Mate grounding wire to the bottom of the baseplate, run to crossbolt hole		
Fasten the crossbolt and nut, clamping one end of the grounding wire		
Adjust rotor to face the mouth of wind tunnel, fasten set screws		
Mate turbine and load side PCC cables		
Connect emergency stop connection to the load side enclosure		

Connect the 5V supply wall power cable		
Verify turbine-side enclosure relay settings and the linear actuator position		
Verify load-side enclosure relay settings and the indication light of the Arduino		
Verify PCC voltage reading matches expected value		
Verify actuator and relays respond to voltage inputs		
Ramp wind up to 5 m/s and verify CUT_IN to POWER_CURVE transition		
Verify stable operation within the bins and correct behavior with increasing wind speed		
Disconnect load and verify transition to the safety state and that all functions are completed as expected		
Reconnect load and verify return to normal operation (Safety state to rated power state) + (ensure all state functions are complete)		
Press E-stop and verify immediate transition to safety state via the completed functions, confirming all deceleration		
Turn off the wind tunnel. After wind has stopped, release E-STOP		

4 Testing Results

Table 5. Testing Results of the Maxon 633919

Wind Speed (m/s)	5	6	7	8	9	10	**Overall**
Score	0.972	2.294	3.783	5.114	4.673	4.320	**21.1566**

Prototype testing was conducted periodically in Virginia Tech's Goodwin wind tunnel to evaluate power output, control response, and system stability across condition ranges. Testing validated cut-in performance, FSM transitions, and rated power regulation, allowing for the system to be tuned and refined. The complete power curve performance of the Maxon 633919 generator and final rotor design is shown in Table 5, where the team was able to exceed the desired score of 20 points outlined in the design objectives by finding optimal load values for each wind speed. Of note is the 10 m/s transition point, where the DC/DC converter was successfully turned on and began outputting a stable power of 14.4 W in preparation for the control of rated power task, while maintaining a safe RPM of ~1600. Structures were repeatedly exposed to much higher angular speeds during DC/DC converter testing, when the system would temporarily enter no-load conditions if an over-current protection mode was triggered. In these scenarios, pitching the blades to the safety angle was able to safely stop the turbine near-instantaneously.

References

Actuonix Motion Devices Inc. 2023. "S20 Series Linear Stepper Actuator Datasheet." Actuonix Motion Devices. https://www.actuonix.com/assets/images/datasheets/ActuonixS20Datasheet.pdf.

Khaled, Mohamed, Mostafa M. Ibrahim, Hesham E. Abdel Hamed, and Ahmed F. AbdelGwad. 2019. "Investigation of a Small Horizontal-Axis Wind Turbine Performance with and without Winglet." Energy 187: 115921. https://doi.org/10.1016/j.energy.2019.115921.

Mourad, Mina G., Tarek A. Mekhail, Ibrahim Shahin, Samir S. Ayad, and Osama E. Abdellatif. 2020. "Effect of Winglet Geometry on Horizontal Axis Wind Turbine Performance." Engineering Reports 2: e12101. https://doi.org/10.1002/eng2.12101.

SKF Group. n.d. "Deep Groove Ball Bearings – Loads." SKF. https://www.skf.com/us/products/rolling-bearings/ball-bearings/deep-groove-ball-bearings/loads.

Maxon EC-i 52 ∅52 mm, brushless, 420 watt. (2026). Maxongroup.co.uk. https://www.maxongroup.co.uk/medias/sys_master/root/9406692622366/Cataloge-Page-EN-315.pdf

Tic T825 USB Multi-Interface Stepper Motor Controller. (2026). Pololu.com. https://www.pololu.com/product/3131

5V 1 Channel Relay Module With optocoupler Support High or Low Level Trigger. (2018). Hiletgo.com. http://www.hiletgo.com/ProductDetail/1958599.html